Effects of spin on magnetized binary neutron star mergers and jet launching

Milton Ruiz,[1] Antonios Tsokaros,[1] Vasileios Paschalidis,[2] and Stuart L. Shapiro[1,3]
[1]Department of Physics, University of Illinois at Urbana-Champaign, Urbana, Illinois 61801, USA
[2]Departments of Astronomy and Physics, University of Arizona, Tucson, Arizona 85719, USA
[3]Department of Astronomy & NCSA, University of Illinois at Urbana-Champaign, Urbana, Illinois 61801, USA

(Received 21 February 2019; published 17 April 2019)

Events GW170817 and GRB 170817A provide the best confirmation so far that compact binary mergers where at least one of the companions is a neutron star can be the progenitors of short gamma-ray bursts (sGRBs). An open question for GW170817 remains the values and impact of the initial neutron star spins. The initial spins could possibly affect the remnant black hole mass and spin, the remnant disk, and the formation and lifetime of a jet and its outgoing electromagnetic Poynting luminosity. Here we summarize our general relativistic magnetohydrodynamic simulations of spinning, neutron star binaries undergoing merger, and delayed collapse to a black hole. The binaries consist of two identical stars, modeled as $\Gamma = 2$ polytropes, in quasicircular orbit, each with spins $\chi_{\rm NS} = -0.053$, 0, 0.24, or 0.36. The stars are endowed initially with a dipolar magnetic field extending from the interior into the exterior, as in a radio pulsar. Following the merger, the redistribution of angular momentum by magnetic braking and magnetic turbulent viscosity in the hypermassive neutron star (HMNS) remnant, along with the loss of angular momentum due to gravitational radiation, induces the formation of a massive, nearly uniformly rotating inner core surrounded by a magnetized Keplerian disklike envelope. The HMNS eventually collapses to a black hole, with spin $a/M_{\rm BH} \simeq 0.78$ independent of the initial spin of the neutron stars, surrounded by a magnetized accretion disk. The larger the initial neutron star spin the heavier the disk. After $\Delta t \sim 3000M - 4000M \sim 45(M_{\rm NS}/1.625\ M_\odot)$ ms $- 60(\mathrm{M_{NS}}/1.625\ \mathrm{M_\odot})$ ms following merger, a mildly relativistic jet is launched. The lifetime of the jet $[\Delta t \sim 100(M_{\rm NS}/1.625\ M_\odot)$ ms $- 140(M_{\rm NS}/1.625\ M_\odot)$ ms] and its outgoing Poynting luminosity $[L_{\rm EM} \sim 10^{51.5\pm1}$ erg/s] are consistent with typical sGRBs, as well as with the Blandford-Znajek mechanism for launching jets and their associated Poynting luminosities.

DOI: 10.1103/PhysRevD.99.084032

I. INTRODUCTION

The gravitational wave (GW) detection GW170817 [1] coincident with electromagnetic (EM) counterpart radiation across the EM spectrum and, in particular, the detection of the short gamma-ray burst (sGRB) 1.7s following the inferred merger time by the Fermi Gamma-Ray Burst Monitor [2] and INTEGRAL [3,4] (event GRB 170817A), provide the best confirmation so far that compact binary mergers, in which at least one of the binary companions is a neutron star, can be the progenitors of sGRBs, as anticipated in [5–7]. We recently demonstrated this possibility by self-consistent simulations in full general relativistic magneto-hydrodynamics (GRMHD) of merging black hole-neutron star (BHNS) binaries [8,9] and merging neutron star binaries (NSNS) [10,11]. Depending on the spin priors of the binary companions, the GW170817 inferred masses are in the broad range of 0.86 $M_\odot$–2.26 $M_\odot$, though the total mass of the system is constrained to be 2.73 $M_\odot$–3.29 $M_\odot$ with 90% credibility [1]. These masses are consistent with astrophysical observations of NSs (see e.g., [12,13] and references therein) which, along with the optical counterparts [2–4,14], indicate the presence of matter, and hence strongly suggest the coalescence of a NSNS as the progenitor of GW170817, although it cannot rule out the possibility that one of the binary companions is a stellar-mass BH (see e.g., [15–18]).

The GRMHD simulations of BHNSs reported in [8,9], in which the NS is modeled as an irrotational $\Gamma = 2$ polytrope, showed that an incipient jet—a collimated, mildly relativistic outflow which is magnetically dominated [i.e., $b^2/(2\rho_0) > 1$, where $b^2 = B^2/4\pi$, ρ_0 is the rest-mass density, and $B^2 = B_i B^i$, with B^i the magnetic field]—may be launched from the highly spinning BH + disk remnant if as follows: (a) the NS is endowed with a magnetic field that extends from the stellar interior into the exterior, as in a radio pulsar; (b) the tilt angle between the magnetic moment and the total angular momentum of the system is small; and (c) the initial BH spin satisfies $a/M_{\rm BH} \gtrsim 0.4$.

Note that the GRMHD simulations in [8,9] do not account for all the physical processes involved in BHNS mergers, such as a realistic finite-temperature nuclear equation of state (EOS) and neutrino processes. It has

been suggested that neutrino pair annihilation in BH + disk engines may carry away a significant amount of energy from inner regions of the disk that may be strong enough to power jets [19–23], though their typical energies and durations might be too small to explain the majority of sGRBs [23]. Recently, it was suggested in [24] that the emergence of a jet in a slowly spinning BH + disk engine may be dominated initially by neutrino pair annihilation followed by the Blandford-Znajek (BZ) [25] process, leading to a transition from a thermally dominated fireball to a Poynting dominated outflow as observed in some GRBs such as GRB 160625B [26].

On the other hand, the GRMHD studies reported in [10,11], where the NS is modeled as an irrotational $\Gamma = 2$ polytrope, showed that NSNS systems may launch an incipient jet whether the seeded poloidal magnetic field is confined to the NS interior or not as long as the binary undergoes a delayed collapse to a BH [27]. The lifetime of the jet [$\Delta t \sim 100(M_{\rm NS}/1.625\ M_\odot)$ ms] and the outgoing electromagnetic luminosities [$L_{\rm EM} \sim 10^{51}$ erg/s] in the above cases turn out to be consistent with short-duration sGRBs [32–34]. Note that the GRMHD simulations reported in [35,36], where the effects of different EOSs, different mass ratios, and different orientations of a poloidal magnetic field confined to the NS interior were probed, and a lack of an outgoing outflow or jet was observed, though formation of an organized magnetic field structure above the BH was evident (see e.g., Fig. 9 in [35]). It is likely that the lack of a jet is due to an insufficient resolution to properly capture the magnetic instabilities that boost the magnetic field strength to $\gtrsim 10^{15.5}$ G, an essential ingredient for jet launching [8,10]. On the other hand, the very high resolution NSNS mergers reported in [37], where NSs are modeled by an H4 EOS and endowed with a poloidal magnetic field confined to the NS interior, did not find any evidence of a magnetically driven outflow after about ∼39 ms following the merger. The lack of a jet in these studies has been attributed to the persistent fallback debris in the atmosphere, which increases the ram pressure above the BH poles. Therefore, a longer simulation is likely required for jet launching. Moreover, the emergence of a jet may be possible only for EOSs for which the matter fallback timescale is shorter than the accretion disk lifetime [38]. Note that heating induced by neutrino pair annihilation in NSNS mergers is not efficiently translated into relativistic outflows and, therefore, neutrinos may not be strong enough to power jets by themselves [23,39].

Due to the limited sensitivity of the second observing run (O2) of Advanced LIGO [1,14], and assuming that the progenitor of GW170817 is the merger of a NSNS system, there is no current consensus yet whether the GW170817 remnant is a highly spinning BH + disk or a long-lived supramassive NS (SNS). Depending on the EOS, NSNS mergers may yield a remnant that can form a long-lived SNS, a transient differentially rotating hypermassive NS (HMNS) that can survive for many rotation periods, or promptly collapse to a BH [40–42]. It was argued in [43] that a transient HMNS can produce both blue and red kilonova ejecta expanding at mildly relativistic velocities, consistent with observations of GW170817 [2–4,14]. This hypothesis is supported by the GRMHD NSNS merger simulations in [10,11,44] where a magnetized HMNS remnant undergoing delayed collapse and not a SNS appears to be a prerequisite for jet launching. This requirement allows us to impose a bound on the maximum mass of a spherical NS: $M_{\rm max}^{\rm sph} \lesssim 2.74/\beta$ [44]. Here β is the ratio of the maximum mass of a uniformly rotating star over the maximum mass of a nonrotating star. Causality arguments allow β to be as high as 1.27 [45,46], while most realistic candidate EOSs predict $\beta \sim 1.2$ (which is approximately EOS independent) yielding $M_{\rm max}^{\rm sph}$ in the range 2.16 $M_\odot$–2.28 $M_\odot$ [44], consistent with estimates arrived at from other considerations [43,47,48]. By contrast, a broad number of GR hydrodynamic simulations favoring a long-lived, massive SNS surrounded by a torus was summarized in [47] to support their inferred requirement of a strong neutrino emitter that has a sufficiently high electron fraction to avoid an enhancement of the ejecta opacity. Recently, it was shown in [49] that a long-lived SNS remnant is fully consistent with the multiwavelength afterglow data taken by different EM observatories 150 days after the GW170817 detection.

The LIGO/Virgo observations of GW170817 practically left the premerger NS spins unconstrained. These could have a strong impact on the remnant disk, the final BH spin, the lifetime of the transient HMNS, the amount of ejected neutron rich matter that can power kilonovae and synthesize heavy elements, as well as the formation and lifetime of a magnetically driven jet and the associated outgoing EM Poynting luminosity. Addressing these issues, GRMHD simulations in the dynamical spacetimes of spinning NSNSs are necessary. Understanding the aforementioned aspects may explain or give new insight regarding sGRB phenomenology and the synergy between EM and GW observations. Prior work on spinning NSNSs, but without magnetic fields, has been presented in [50–54] with a constraint satisfying initial data, and in [55,56] with a constraint violating initial data (see also [57] for work in the conformal flatness approximation). Work has also been performed on eccentric binaries with spinning NSNSs and a constraint satisfying initial data [58–61].

With respect to the spin of the BH which was formed after the collapse of the merger remnant, Refs. [55,56] found that it increases as the spin of the NSs in the binary increase. In particular, the authors of [55] investigate NSs with a $\Gamma = 2$ EOS and spins that range from -1 up to 1.2 times the spin that corresponds to the corotating solution, and they find a ∼10% increase in the BH spin. Similar results were reported in [56] with more realistic EOSs. A prompt collapse to a BH is possible only if the mass of

the NSs in the binary is above a certain threshold, which depends on the EOS. This highlights the fact that if the total mass of the binary is close to the critical mass for prompt collapse, the spin of the NSs can have a strong impact on the dynamics of the merger.

Here we initiate new investigations by performing fully relativistic GRMHD simulations of *magnetized* and *spinning* NSNS configurations in a quasicircular orbit that undergo delayed collapse to BH. The binaries are formed by two identical spinning NSs modeled by a $\Gamma = 2$ polytropic EOS and spins $\chi_{\rm NS} \equiv J_{\rm ql}/(M/2)^2 = -0.053$, 0, 0.24, 0.36, where $J_{\rm ql}$ is the quasilocal angular momentum of the NS, and M is the Arnowitt-Deser-Misner (ADM) mass of the system [62]. Denoting by $\Sigma_{\rm cor}$ the circulation that corresponds to the corotating binary with the same ADM mass and at the same separation, these spins correspond to circulations of $-0.3\Sigma_{\rm cor}$, $\Sigma_{\rm cor}$, $1.6\Sigma_{\rm cor}$. The stars are initially threaded by a dipolar magnetic field extending from the stellar interior into the exterior, as in radio pulsars [10]. To determine the impact of the magnetically driven instabilities on the fate of spinning NSNS mergers, we also consider unmagnetized evolutions of the above NSNS configurations.

We find that, following a merger, the redistribution of angular momentum by magnetic braking due to winding and magnetic turbulence driven by the magnetorotational instability (MRI) in the HMNS remnant, along with the dissipation of angular momentum due to gravitational radiation, induces the formation of a massive, nearly uniformly rotating inner core surrounded by a magnetized, Keplerian, disklike envelope (similar behavior has been reported in supermassive stars modeled by a polytropic EOS with $\Gamma \gtrsim 4/3$ in [63]). In all cases, by $t - t_{\rm mer} \sim 15(M_{\rm NS}/1.625\ M_\odot)$ ms $- 20(M_{\rm NS}/1.625\ M_\odot)$ ms following a merger, the HMNS collapses to a BH. Interestingly, we find that the nascent BH spin is $a/M_{\rm BH} \simeq 0.78$ independent of the initial NS spin. The final BH is surrounded by an accretion disk whose rest mass depends strongly on the initial spin of the NSs. We observe that the larger the initial spin, the heavier the disk. In contrast to the magnetized cases which form a black hole, in the unmagnetized cases, only the HMNS remnant of the antialigned ($\chi_{\rm NS} = -0.053$) and the irrotational configurations (those with less centrifugal support) collapse to a BH during the time evolved [in $t - t_{\rm mer} \sim 15(M_{\rm NS}/1.625\ M_\odot)$ ms]. This is in agreement with the pure hydrodynamic simulations of [55] whose lowest mass model ($M_{\rm NS} = 1.63\ M_\odot$ in their notation, compared to our $1.5\ M_\odot$ model) reaches a quasistationary state, with the BH mass and spin changing less than 0.4% during the last $t \sim 50\ M_{\rm BH}$ for all their simulations and with negligible mass accretion. In our other two cases, the HMNS remnant is driven to a quasiaxisymmetric configuration on a dynamical timescale and remains in quasistationary equilibrium until the termination of our simulations [$t - t_{\rm mer} \gtrsim 60(M_{\rm NS}/1.625\ M_\odot)$ ms]. Angular momentum loss due to gravitational radiation alone is, therefore, an inefficient mechanism to trigger the collapse of a highly spinning HMNS. Other dissipation, such as turbulent viscosity or magnetic fields, will lead to collapse, but only on a longer timescale.

After $\Delta t \sim 3000M - 4000M \sim 45(M_{\rm NS}/1.625 M_\odot)$ ms$-$ $60(M_{\rm NS}/1.625\ M_\odot)$ ms following a merger, a magnetically driven and sustained incipient jet is launched. The lifetime of the jet [$\Delta t \sim 100(M_{\rm NS}/1.625\ M_\odot)$ ms $- 140(M_{\rm NS}/1.625\ M_\odot)$ ms] and its respective outgoing EM Poynting luminosity [$L_{\rm EM} \sim 10^{51.5\pm1}$ erg/s] turn out to be consistent with typical short-duration sGRBs (see e.g., [32–34]), as well as with the BZ process for launching jets and their associated Poynting luminosities. We also find that the ejecta in the high spin NSNS configurations (aligned cases) is $\sim 10^{-2.2}\ M_\odot$ and, therefore, can give rise to the so-called kilonova event that can be detected by current telescopes, as well as the Large Synoptic Survey Telescope (LSST) [47,64].

The remainder of the paper is organized as follows. A short summary of the numerical methods and their implementation is presented in Sec. II. A detailed description of the adopted initial data and the grid structure used to solve the GRMHD equations are given in Secs. II A and II B, respectively. In Sec. II C we describe the diagnostics employed to monitor and verify the reliability of our numerical calculations. We present our results in Sec. III. Finally, we summarize our findings and conclusions in Sec. IV. Throughout the paper we adopt geometrized units ($G = c = 1$) except where stated explicitly. Greek indices denote all four spacetime dimensions, while latin indices imply spatial parts only.

II. METHODS

We use the extensively tested Illinois GRMHD code which is embedded in the CACTUS infrastructure [65,66]. The code evolves the Baumgarte-Shapiro-Shibata-Nakamura (BSSN) equations [67,68] (for a detailed discussion see also [69]) with fourth order centered spatial differencing, except on shift advection terms, where a fourth order upwind differencing is used. Outgoing wavelike boundary conditions are applied to all BSSN evolved variables. These variables are evolved using the equations of motion (9)–(13) in [70], along with the $1 + \log$ time slicing for the lapse α and the "Gamma-freezing" condition for the shift β^i, cast in first order form [see Eqs. (2)–(4) in [70]]. For numerical stability, we set the damping parameter η appearing in the shift condition to $\eta = 3.75/M$, with M the ADM mass of the system. For additional stability we modify the equation of motion of the conformal factor ϕ by adding a dissipation term [see Eq. (19) in [71]] which damps the Hamiltonian constraint. During the whole evolution we set the constraint damping parameter to $c_H = 0.04$. The time integration is performed via the method of lines using a fourth-order accurate Runge-Kutta

integration scheme with a Courant-Friedrichs-Lewy (CFL) factor set to 0.5. We use the CARPET infrastructure [72,73] to implement the moving-box adaptive mesh refinement. Fifth order Kreiss-Oliger dissipation [74] has also been added in the BSSN evolution equations.

For matter and magnetic field evolution, the code solves the equations of ideal GRMHD in a conservative scheme via high-resolution shock capturing methods. The conservative variables are evolved through Eqs. (27)–(29) in [75]. To ensure the magnetic field remains divergence-less during the evolution, we integrate the magnetic induction equation using a vector potential $\mathcal{A}^\mu$ [see Eqs. (19)–(20) in [75]]. We adopt the generalized Lorenz gauge described in [76] to avoid the appearance of spurious magnetic fields [77]. The damping parameter is set to $\xi \approx 6.5/M$. We employ a Γ-law EOS $P = (\Gamma - 1)\rho_0\epsilon$ and allow for shock heating. Here ϵ is the specific internal energy and ρ_0 is the rest-mass density. In all our models we set $\Gamma = 2$.

A. Initial data

We consider unmagnetized and magnetized NSNS configurations in a quasiequilibrium circular orbit that inspiral, merge, and undergo delayed collapse to a BH. The binaries consist of two identical NSs modeled by a polytropic EOS with $\Gamma = 2$. Each binary companion has an initial spin of $\chi_{\rm NS} = -0.05$, 0.24, or 0.36. Our extreme case corresponds to a binary in which the NSs have an initial rotation period of $\sim 2.3(M_{\rm NS}/1.625\ M_\odot)$ ms (see Table I).

The initial data are computed using the COMPACT OBJECT CALCULATOR (COCAL) [62,78], and their main properties are listed in Table I. Following [10], we rescale the rest mass of the stars to $M_{\rm NS} = 1.625\ M_\odot (k/k_L)^{1/2}$ where $k_L = 269.6$ km^2 is the polytropic constant used to compute the initial data, and $k = P/\rho_0^\Gamma$. In all cases the binaries have ADM mass $M = 4.43(M_{\rm NS}/1.625\ M_\odot)$ km and an initial coordinate separation of $45(M_{\rm NS}/1.625\ M_\odot)$ km. A single isolated spherical star with mass $M_{\rm TOV} = M/2$ has compactness $\mathcal{C} = 0.138$, second Love number $k_2 = 0.0807$ [79,80], and tidal deformability $\Lambda = (2/3)k_2\mathcal{C}^{-5} = 1080$. Notice that for this EOS with $\Gamma = 2$ the maximum mass configuration has a $\mathcal{C} = 0.21$, and $M_{\rm NS}^{\rm max} = 1.23 M_{\rm NS}$. The tag in Table I for each configuration is formed by the spin direction (sp = aligned and sm = antialigned) followed by its magnitude. For comparison purposes, we also consider the NSNS P-case treated previously in [10] and denoted here as irrot. To distinguish between hydrodynamic or magnetized evolutions, an "H" or "M" will precede the tag, respectively.

TABLE I. Summary of the initial properties of the NSNS configurations. The binaries have ADM mass M and ADM angular momentum J, while the NSs have quasilocal dimensionless spin parameter $\chi_{\rm NS} \equiv J_{\rm ql}/(M/2)^2$ which is either aligned or antialigned with respect to the total angular momentum of the system, approximate rotational period T in units of $(M_{\rm NS}/1.625\ M_\odot)$ ms [62], coordinate equatorial radius toward companion R_x, and coordinate polar radius R_z in units of $(M_{\rm NS}/1.625\ M_\odot)$ km. In all cases, the orbital separation is fixed at $D_0 = 45(M_{\rm NS}/1.625\ M_\odot)$ km, corresponding to an initial angular velocity of $M\Omega_0 \simeq 0.027$. The tag for each configuration is formed by the spin direction (sp = aligned and sm = antialigned) followed by its magnitude. For comparison purposes, we also consider the irrotational P-configuration treated previously in [10] and denoted here as irrot.

Model	J/M^2	$\chi_{\rm NS}$	T [ms]	R_x [km]	R_z [km]
sp0.36	1.14	0.36	2.3	15.00	13.77
sp0.24	1.09	0.24	3.2	14.19	13.18
sm0.05	0.95	−0.05	−12.0	13.67	12.63
irrot	0.98	0.0	0.0	13.67	12.73

In the magnetized cases, the stars are initially seeded with a dynamically unimportant dipolelike magnetic field generated by the vector potential [76,81]

$$A_\phi = \frac{\pi \varpi^2 I_0 r_0^2}{(r_0^2 + r^2)^{3/2}} \left[1 + \frac{15 r_0^2 (r_0^2 + \varpi^2)}{8(r_0^2 + r^2)^2}\right] \qquad (1)$$

that approximately corresponds to that induced by an interior current loop with radius r_0 and current I_0. Here $r^2 = \varpi^2 + z^2$, with $\varpi^2 = (x - x_{\rm NS})^2 + (y - y_{\rm NS})^2$, and $(x_{\rm NS}, y_{\rm NS})$ is the position of the maximum value of the rest-mass density of the NS. As in [10], we choose I_0 and r_0 such that the maximum value of the magnetic-to-gas-pressure ratio in the NS interior is $\beta^{-1} \equiv P_{\rm mag}/P_{\rm gas} = 0.003125$. The initial magnetic field strength at the NS pole turns out to be $B_{\rm pole} \sim 10^{15.2}(1.625\ M_\odot/M_{\rm NS})$ G. This strength has been chosen in [10] to mimic the growth of the magnetic field due to the Kelvin-Helmholtz (KH) instability and the MRI triggered during the NSNS merger and HMNS phase of the evolution recently reported in the very high resolution NSNS simulations in [82]. There it was found that during merger the rms magnetic field strength is boosted from $\sim 10^{13}$ G to $\sim 10^{15.5}$ G, with local values up to $\sim 10^{17}$ G.

Following [10], to reliably evolve the exterior magnetic field and, at the same time, mimic magnetic-pressure dominance that characterizes the likely force-free, pulsar-like exterior magnetosphere, we initially enforced a low and variable density in regions where magnetic field stresses dominate over the fluid pressure gradient [see Eq. (4) in [9]], such that the magnetic-to-gas-pressure ratio in the NS exterior is $\beta_{\rm ext}^{-1} = 100$, which increases the total rest mass of the system by $\lesssim 0.5\%$. For the subsequent evolution, we integrate the ideal GRMHD equations everywhere imposing a density floor in regions where $\rho_0^{\rm atm} \leq 10^{-10}\rho_0^{\rm max}$, where $\rho_0^{\rm max}$ is the initial maximum density of the NS, as is typically done in hydrodynamics schemes to recover the so-called primitive variables (see e.g., [83]).

TABLE II. Grid hierarchy in units of M for models listed in Table I. The computational mesh consists of two sets of seven nested refinement boxes, the innermost ones centered on each star. The finest box around the NS has a half-length of $\sim 1.3R_{\rm NS}$, where $R_{\rm NS}$ is the initial stellar radius. The number of grid points covering the equatorial radius of NS is denoted by $N_{\rm NS}$. In terms of grid points per NS radius the resolution used here is slightly larger than that in [10]. In all cases, we impose symmetry about the orbital plane.

Model	Grid hierarchy (half-length)	Max. resolution	$N_{\rm NS}$
sp0.36	(266.74, 133.37, 66.68, 33.34, 16.67, 8.33, 4.17)	$0.05M$	66
sp0.24	(252.34, 126.17, 63.08, 31.34, 15.77, 7.88, 3.94)	$0.05M$	66
sm0.05	(243.10, 121.54, 60.77, 30.38, 15.19, 7.60, 3.80)	$0.05M$	66
irrot[a]	(246.15, 123.76, 61.53, 30.77, 15.38, 7.70, 3.84)	$0.05M$	61

[a]P-case configuration treated previously in [10].

B. Grid structure

The grid hierarchy used in our simulations is summarized in Table II. It consists of two sets of seven nested refinement boxes, the innermost ones centered on each star. Once they overlap, they are replaced by a common box centered on the system center of mass. Each set consists of seven boxes that differ in size and in resolution by factors of 2. The finest box around the star has a side half-length of $\sim 1.3R_{\rm NS}$, where $R_{\rm NS}$ is the initial NS equatorial radius (see Table I). In all cases, the initial NS radius is resolved by ∼66 grid points. We impose reflection symmetry across the orbital plane. Note that this resolution matches the medium resolution used in [10], although in terms of grid points per NS radius the resolution used here is slightly larger.

C. Diagnostics

To verify how close to equilibrium our initial NSNS configurations are, we monitor the maximum value of the rest-mass density ρ_0 during the early inspiral and find oscillations with an amplitude of about $\lesssim 1\%$ even in our highest spinning case ($\chi_{\rm NS} = 0.36$), as displayed in Fig. 1.

On the other hand, to validate our numerical results, we monitor the L_2 normalized constraints computed via Eqs. (40)–(41) in [70]. We find that during the inspiral and after the formation of the HMNS the constraints oscillate around 1%–2%. During NSNS merger and BH formation, they peak at $\lesssim 6\%$ in the pure hydrodynamic cases and at $\lesssim 8\%$ in the magnetized cases. After that point, the constraints settle back to $\lesssim 0.1\%$.

The BH apparent horizon is located and monitored through the AHFinderDirect thorn [84]. We estimate the BH mass $M_{\rm BH}$ and the BH dimensionless spin parameter $a/M_{\rm BH}$ using the isolated horizon formalism [85]. To measure the flux of energy and angular momentum carried away by GWs, we use a modified version of the Psikadelia thorn that computes the Weyl scalar Ψ_4, which is decomposed into $s = -2$ spin-weighted spherical harmonics [86] at different radii between $r_{\rm min} \approx 30M \sim 133(M_{\rm NS}/1.625\ M_\odot)$ km and $r_{\rm max} \approx 170M \sim 752(M_{\rm NS}/1.625\ M_\odot)$ km. We find that between ∼0.8% and ∼1.4% of the total energy of our NSNS models is radiated away during the evolution in form of gravitational radiation, while between ∼12% and ∼19% of the angular momentum is radiated (see Table III). The escaping mass (ejecta) is computed via $M_{\rm esc} = \int \rho_* d^3x$ outside a coordinate radius $r > r_0$, and under the conditions that follow: (a) $-1 - u_t > 0$ (fluid particle energy per unit rest mass), and (b) the radial velocity of the ejected material $v^r > 0$. Here $\rho_* \equiv -\sqrt{\gamma}\rho_0 n_\mu u^\mu$. Varying r_0 between $30M \approx 133(M_{\rm NS}/1.625\ M_\odot)$ km and $r_{\rm max} \approx 100M \sim 443(M_{\rm NS}/1.625\ M_\odot)$ km, we checked that the ejecta masses we report are independent of r_0. Between 0.02% and 0.14% of the total rest mass of the system is ejected. Notice that ejecta masses of ∼0.1% or greater are required for detectable kilonovae by current or planned telescopes, such as LSST [87].

We also monitor the conservation of both the interior mass $M_{\rm int}$ and the interior angular momentum $J_{\rm int}$ of the system contained in the numerical domain via Eqs. (19)–(22) in [89]. These quantities coincide with the ADM mass and ADM angular momentum of the system at spatial

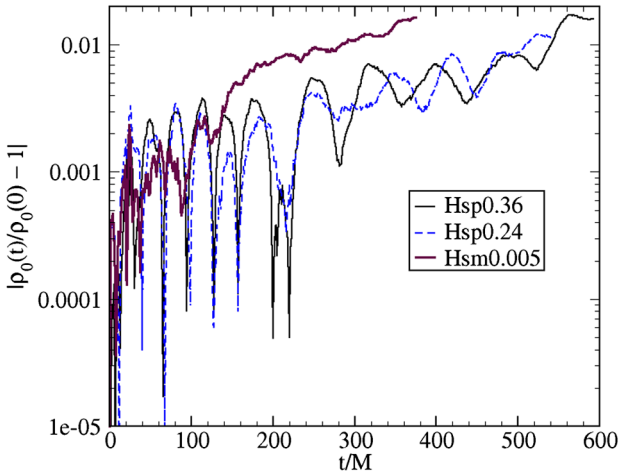

FIG. 1. Maximum value of the rest mass $\rho_0(t)$ during the early inspiral, normalized by the initial maximum density $\rho_0(0)$, for the unmagnetized cases (see Table I). In all cases, the NS oscillations are $\lesssim 1\%$, and they are more pronounced in the antialigned case (Hsm0.005 configuration).

TABLE III. Final outcomes. Here $t_{\rm mer}$, $t_{\rm BH}$, and $t_{\rm evo}$ are the NSNS merger time, the BH formation time measured after merger, and the full evolution time, respectively. All of them are in units of $(M_{\rm NS}/1.625\ M_\odot)$ ms. The mass and the dimensionless spin parameter of the remnant BH are $M_{\rm BH}$ and $\tilde{a} \equiv a/M_{\rm BH}$, respectively; $M_{\rm disk}$ is the rest mass of the accretion disk near the end of the simulation; $\dot{M}$ is the rest-mass accretion rate computed via Eq. (A11) in [88] in units of $(M_\odot/s)$; $\tau_{\rm disk} \sim M_{\rm disk}/\dot{M}$ is the disk lifetime (lifetime of the jet, if any) in units of $(M_{\rm NS}/1.625\ M_\odot)$ s; $M_{\rm esc}$ denotes the escaping mass; $\Delta\bar{E}_{\rm GW} \equiv \Delta E_{\rm GW}/M_{\rm ADM}$ and $\Delta\bar{J}_{\rm GW} \equiv \Delta J_{\rm GW}/J_{\rm ADM}$ are the fractions of the total energy and total angular momentum carried away by GWs, respectively; $\alpha_{\rm SS}$ is the Shakura-Sunyaev viscosity parameter; $B_{\rm rms}$ denotes the rms value of the magnetic field above the BH poles in units of $(1.625\ M_\odot/M_{\rm NS})$ G; $L_{\rm EM}$ is the Poynting luminosity in erg/s driven by the incipient jet; and $\eta_{\rm eff} = L_{\rm EM}/\dot{M}$ is the jet efficiency. These last two quantities are time averaged over the last $500M \sim 7.4(M_{\rm NS}/1.625\ M_\odot)$ ms before the termination of our simulations. Finally, Γ_L is the maximum fluid Lorentz factor near $t_{\rm evo}$. [N/A] denotes "not applicable."

Model	$t_{\rm mer}$	$t_{\rm BH}$	$t_{\rm evo}$	$M_{\rm BH}$	$\tilde{a}$	$M_{\rm disk}/M_0$ [a]	$\dot{M}$ [b]	$\tau_{\rm disk}$	$M_{\rm esc}/M_0$ [c]	$\Delta\bar{E}_{\rm GW}$	$\Delta\bar{J}_{\rm GW}$	$\alpha_{\rm SS}$	$B_{\rm rms}$	$L_{\rm EM}$	$\eta_{\rm eff}$	Γ_L
Hsp0.36	11.2	[N/A]	62	[N/A]	[N/A]	0.83%	[N/A]	[N/A]	10^{-4}%	0.8%	12.9%	[N/A]	[N/A]	[N/A]	[N/A]	[N/A]
Hsp0.24	10.7	[N/A]	62	[N/A]	[N/A]	0.74%	[N/A]	[N/A]	10^{-4}%	0.9%	13.5%	[N/A]	[N/A]	[N/A]	[N/A]	[N/A]
Hsm0.05	7.4	13.5	62	2.95 $M_\odot$	0.76	0.55%	0.44	40.6	10^{-5}%	1.4%	18.6%	[N/A]	[N/A]	[N/A]	[N/A]	[N/A]
Msp0.36	8.5	20.5	62	2.75 $M_\odot$	0.78	7.82%	2.71	138.5	0.14%	0.76%	11.55%	0.01–0.09	$10^{15.8}$	$10^{52.1}$	0.26%	1.26
Msp0.24	7.9	20.0	62	2.79 $M_\odot$	0.77	6.65%	2.70	118.2	0.12%	0.76%	12.08%	0.02–0.07	$10^{15.8}$	$10^{52.3}$	0.32%	1.27
Msm0.05	5.6	15.8	77	2.93 $M_\odot$	0.77	1.0%	0.49	97.9	0.02%	1.1%	14.56%	0.01–0.06	$10^{15.7}$	$10^{51.5}$	0.36%	1.21
Hirrot	7.7	15.5	52	2.85 $M_\odot$	0.78	0.81%	0.48	81.0	10^{-5}%	1.3%	16.8%	[N/A]	[N/A]	[N/A]	[N/A]	[N/A]
Mirrot [d]	6.8	18.0	74	2.85 $M_\odot$	0.8	1.0%	0.48	100.0	0.03%	1.0%	14.52%	0.04–0.08	$10^{16.0}$	$10^{51.3}$	0.24%	1.25

[a] M_0 denotes the initial total rest mass of the system.
[b] $\dot{M}$ is reported once the accretion begins to settle into a quasistationary state. So, we quote the accretion rate at $t - t_{\rm BH} \sim 18(M_{\rm NS}/1.625\ M_\odot)$ ms for cases Hsm0.05 and Hirrot, at $t - t_{\rm BH} \sim 15(M_{\rm NS}/1.625\ M_\odot)$ ms for cases Msp0.36 and Msp0.24, and at $t - t_{\rm BH} \sim 20(M_{\rm NS}/1.625\ M_\odot)$ ms for cases Msm0.05 and Mirrot (see Fig. 7).
[c] $M_{\rm esc}$ reported near the termination of our simulations (see inset of Fig. 11).
[d] P-case configuration reported in [10].

infinity. Taking into account the GW radiation losses and the escaping mass we find that, in all the NSNS configurations considered here, the violation of the conservation of $M_{\rm int}$ is $\lesssim 1\%$ along the whole evolution, while the violation of the conservation of $J_{\rm int}$ is $\sim 1\%$ in the antialigned and irrotational cases, and $\lesssim 4\%$ in the other cases. In addition, we monitor the conservation of the rest mass $M_0 = \int \rho_* d^3x$, as well as the magnetic energy growth outside the BH apparent horizon $\mathcal{M} = \int u^\mu u^\nu T^{r({\rm EM})}_{\mu\nu} dV$ as measured by a comoving observer [11].

To probe MHD turbulence in our systems, we compute the effective Shakura-Sunyaev $\alpha_{\rm SS}$ parameter [90] associated with the effective viscosity due to magnetic stresses through $\alpha_{\rm SS} \sim T^{\rm EM}_{\hat{r}\hat{\phi}}/P$ [see Eq. (26) in [91]]. We also verify that the MRI is captured in the post-merger phase of our simulations by computing the quality factor $Q_{\rm MRI} \equiv \lambda_{\rm MRI}/dx$, which measures the number of grid points per fastest growing MRI mode. Here $\lambda_{\rm MRI}$ is the fastest-growing MRI wavelength defined as $\lambda_{\rm MRI} \approx 2\pi\sqrt{|b_P b^P|/(b^2+\rho_0 h)}/|\Omega(r,\theta)|$ where $|b^P| \equiv \sqrt{b^2 - |b_\mu (e_{\hat{\phi}})^\mu|^2}$, and $(e_{\hat{\phi}})^\mu$ is the orthonormal vector carried by an observer comoving with the fluid, $\Omega(r,\theta)$ is the angular velocity of the disk remnant, and dx is the local grid spacing [92]. Note that typically capturing MRI requires $Q_{\rm MRI} \gtrsim 10$ (see e.g., [93,94]). We also compute the outgoing EM Poynting luminosity $L = -\int T^{r({\rm EM})}_t \sqrt{-g} d\mathcal{S}$ across spherical surfaces of coordinate radii between $r_{\rm ext} = 46M \simeq 204(M_{\rm NS}/1.625\,M_\odot)$ km and $190M \simeq 842(M_{\rm NS}/1.625\ M_\odot)$ km. Finally, we monitor the time and azimuthally averaged angular velocity $\Omega(t,r)$ of the HMNS in the equatorial plane as [95,96]

$$\Omega(t,r) = \frac{1}{4\pi P_c}\int_{t-P_c}^{t+P_c}\int_0^{2\pi} \frac{u^\phi}{u^t} dt' d\phi, \qquad (2)$$

where u^t and u^ϕ are components of the four velocity u^μ and P_c is the period of the HMNS at birth, the time at which the two dense cores collide (see below).

III. RESULTS

The basic evolution and final outcome of our new spinning NSNS configurations are similar to those reported in [10]. The binaries start from an inspiral separation of $45(M_{\rm NS}/1.625\ M_\odot)$ km (or ~3–4 orbits before the merger; see the first column in Fig. 2 and the first row in Fig. 3). As the GWs extract energy and angular momentum, the orbital separation shrinks and, depending on the initial spin of the NSs, after about $410M - 750M \sim 8(M_{\rm NS}/1.625\,M_\odot)$ ms–$11(M_{\rm NS}/1.625\,M_\odot)$ ms the stars merge (see the second column in Fig. 2 and the second row in Fig. 3). We define the merger time $t_{\rm mer}$ as the time of peak amplitude of GWs (see Fig. 4). Following the merger, a massive remnant forms with two dense cores rotating about each other that

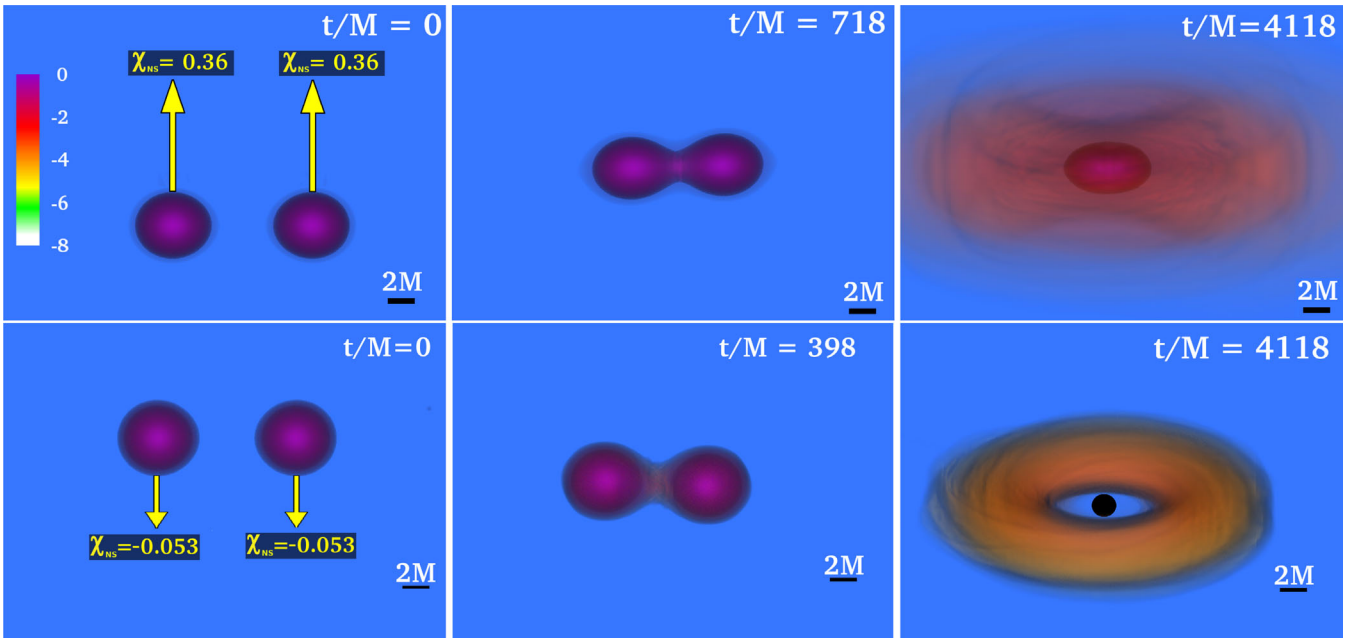

FIG. 2. Volume rendering of rest-mass density ρ_0, normalized to the initial maximum value $\rho_{0,\max} \simeq 10^{14.4}(1.625\ M_\odot/M_{\rm NS})^2\ {\rm g/cm^3}$ (log scale), at selected times for our extreme unmagnetized cases: Hsp0.36 (top panels) and Hsm0.05 (bottom panels). Arrows indicate the direction of the spin. The BH apparent horizon in Hsm0.05 is displayed as a black sphere. Here $M = 1.47 \times 10^{-2}(M_{\rm NS}/1.625\ M_\odot)$ ms $= 4.43(M_{\rm NS}/1.625\ M_\odot)$ km.

eventually collide and become a highly differentially rotating HMNS (see Fig. 5) wrapped in a dense cloud of matter (see the right top panel in Fig. 2 and the third row in Fig. 3). The HMNS is composed by matter with a rest-mass density $\rho_0 \gtrsim 10^{13.5}(1.625\ M_\odot/M_{\rm NS})^2\ {\rm g/cm^3}$. So, as is shown in the third row of Fig. 3, the larger the initial spin of the NSs the denser the matter wrapping around the newborn HMNS. The HMNS has an initial coordinate equatorial radius of roughly $R_{\rm eq} \sim 3.5M \sim 15.5(M_{\rm NS}/1.625\ M_\odot)$ km, polar radius of $R_{\rm pol} \sim 1.5M \sim 6.7(M_{\rm NS}/1.625\ M_\odot)$ km, and a rest mass of $M_0 \simeq 3.2\ M_\odot(M_{\rm NS}/1.625\ M_\odot)$ that exceeds the supramassive limit, i.e., the maximum value allowed for uniformly rotating stars with a $\Gamma = 2$ polytropic EOS, i.e., $M_0 \simeq 2.4(M_{\rm NS}/1.625\ M_\odot)\ M_\odot$ [97,98]. Redistribution of the angular momentum triggered by torques induced by the nonaxisymmetric matter distributions in the star [99], magnetic winding [100], and/or magnetically driven instabilities [63,101], along with dissipation of angular momentum due to gravitational radiation, cause the HMNS to undergo a delayed collapse to a BH (see the bottom panel in Fig. 2 and the fourth row in Fig. 3). By contrast to the unmagnetized cases, where the nascent, highly spinning BH + disk configuration simply settles down (see the bottom panel in Fig. 2), in all the magnetized cases the spinning BH + disk remnant is an engine that launches a magnetically sustained jet whose outgoing EM Poynting luminosity is consistent with sGRBs (see the bottom panels in Fig. 3 and Fig. I in [10]).

In the following section, we describe the final outcome of our NSNS mergers that differ in magnetic field content (unmagnetized and pulsarlike magnetized cases), and in the initial spin of the NSs ($\chi_{\rm NS} = -0.05$, 0.24, and 0.36). For completeness, we also include the irrotational P-case already reported in [10]. Key results from our models are displayed in Table III.

A. Unmagnetized NSNS binaries

As in spinning binary BH mergers, the magnitude and direction of the initial spin of the NSs with respect to the orbital angular momentum affects the merger time $t_{\rm mer}$. The left panel of Fig. 4 displays the GW strain of the dominant mode h_+^{22} as a function of the retarded time at a coordinate extraction radius of $r_{\rm ext} \approx 100 \sim 443(M_{\rm NS}/1.625\ M_\odot)$ km for all cases. The NSNS configurations with spins aligned with the orbital angular momentum (the top and second left panels in Fig. 4) undergo about one more orbit compared to the antialigned and the irrotational cases (the third and bottom panels in Fig. 4), which take around ~3 orbits to merge (see Table III). This so-called orbital hang-up effect is attributed to the spin-orbit coupling [102].

Following the merger, a highly deformed HMNS with a rest mass $M_0 \simeq 3.2(M_{\rm NS}/1.625\ M_\odot)M_\odot$ is formed spinning with a central rotation period that ranges between $\sim 0.24(M_{\rm NS}/1.625\ M_\odot)$ ms, in case Hsp0.36, and $\sim 0.34(M_{\rm NS}/1.625\ M_\odot)$ ms, in case Hsm0.05 (see the top panel in Fig 5). As thermal pressure during the merger is not sufficient [103], and the rest mass of the

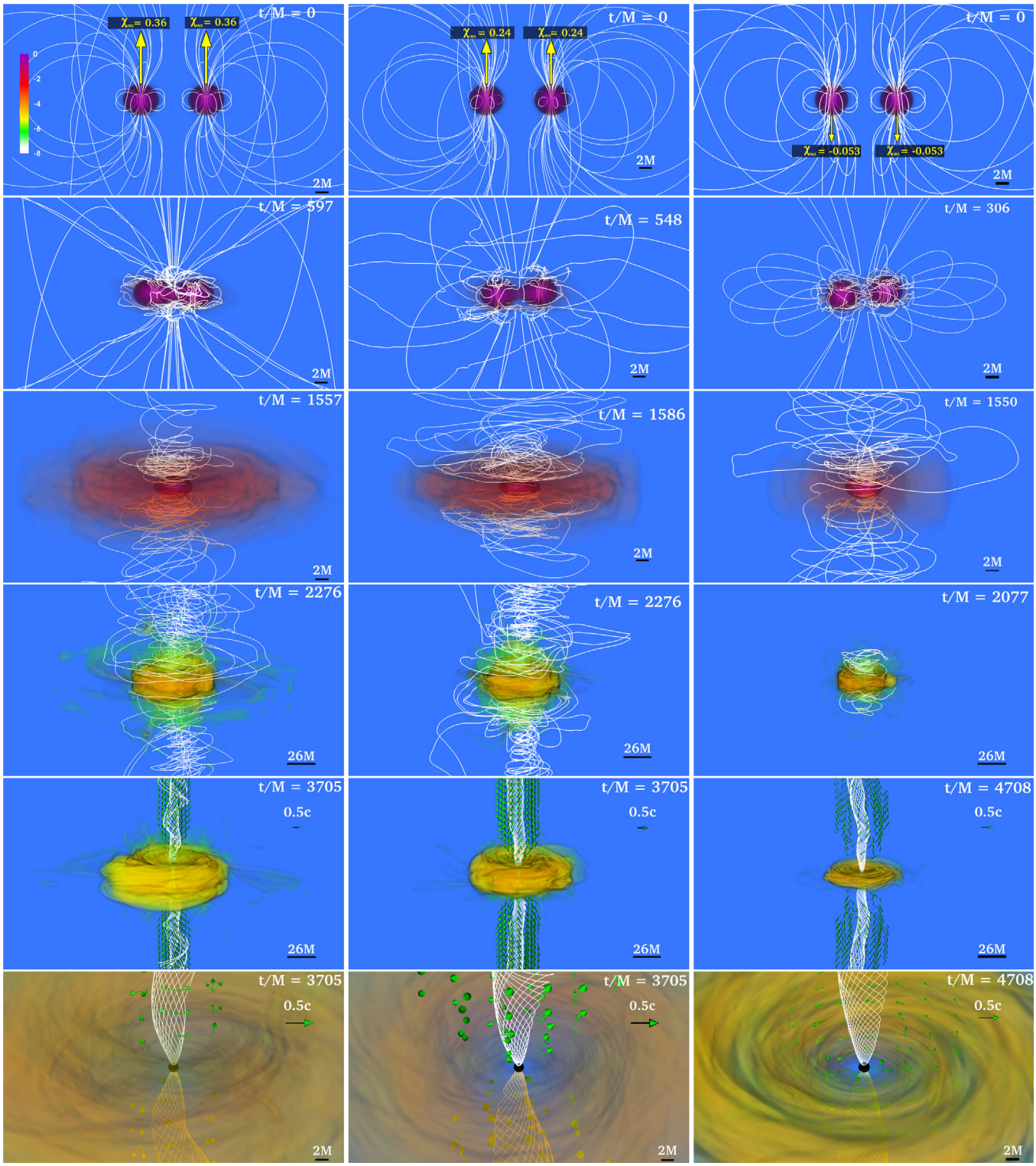

FIG. 3. Volume rendering of rest-mass density ρ_0, normalized to the initial maximum value $\rho_{0,\max} \simeq 10^{14.4}(1.625\ M_\odot/M_{\rm NS})^2\ {\rm g/cm^3}$ (log scale), at selected times for magnetized cases (see Table III): Msp0.36 (left column), Msp0.24 (middle column), and Msm0.05 (right column). See also Fig. 1 in [10]. Bottom panels highlight the system after an incipient jet is launched. Arrows indicate plasma velocities while white lines show the magnetic field structure. The BH apparent horizon is displayed as a black sphere (see bottom panels). Here $M = 1.47 \times 10^{-2}(M_{\rm NS}/1.625M_\odot)$ ms $= 4.43(M_{\rm NS}/1.625M_\odot)$ km.

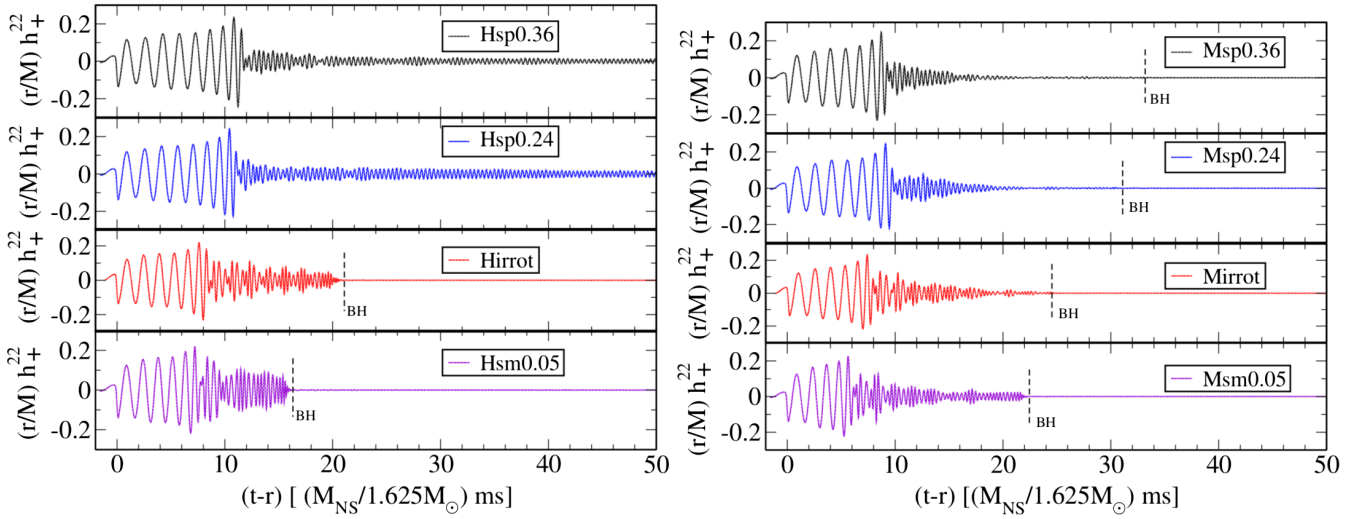

FIG. 4. GW strain h_+^{22} (dominant mode) as functions of retarded time, extracted at $r_{\rm ext} \approx 100M \sim 443(M_{\rm NS}/1.625\ M_\odot)$ km for all cases listed in Table III. The left panel displays the GW strain in the unmagnetized cases, while the right panel displays the magnetized cases. The dashed vertical line denotes the BH formation time.

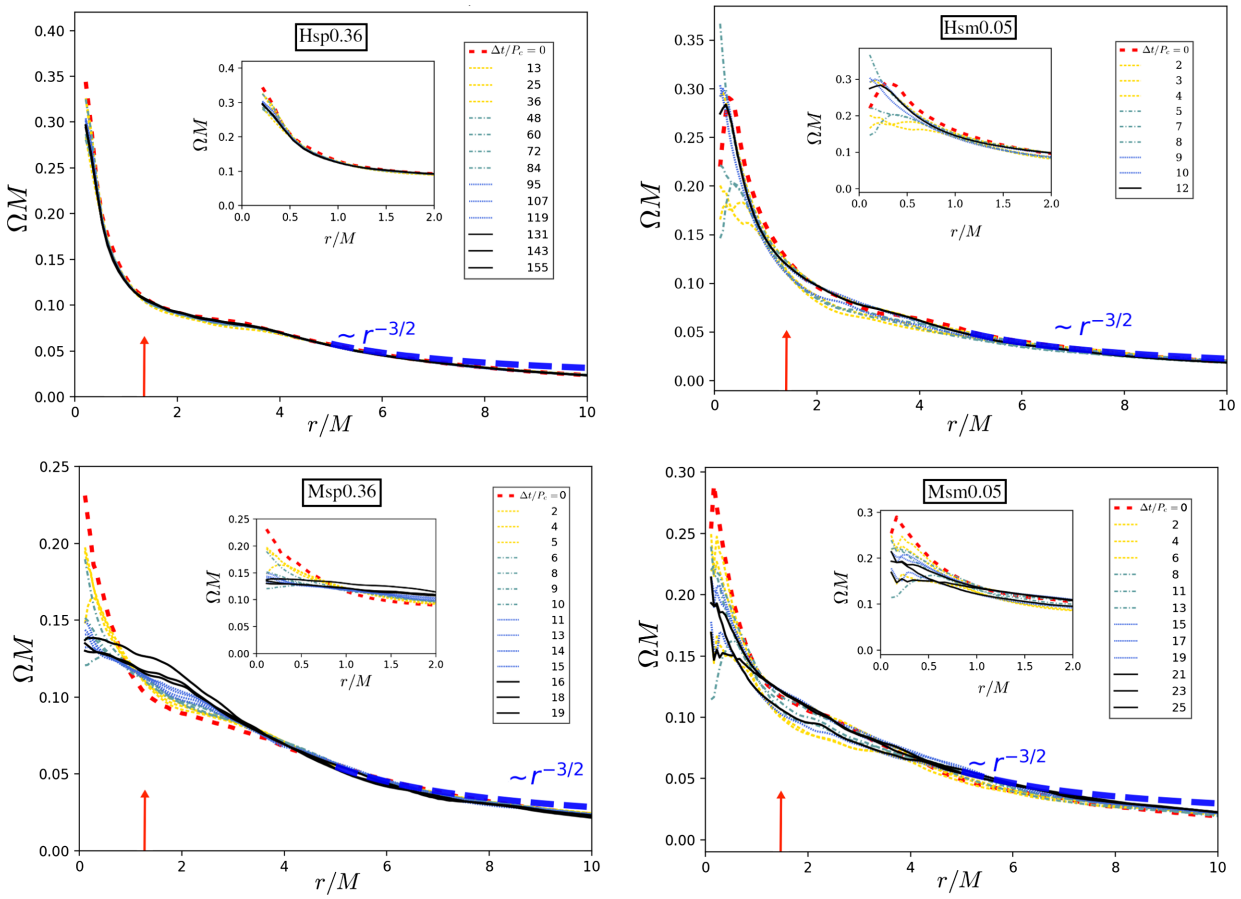

FIG. 5. Angular velocity profile of the HMNS in the equatorial plane at $\Delta t = t - t_{\rm HMNS}$, with $t_{\rm HMNS}$ the HMNS formation time, and P_c the central HMNS period at $t = t_{\rm HMNS}$ [see Eq. (2)] for our extreme cases in Table III (unmagnetized and magnetized cases are shown in top and bottom panels, respectively). The initial differential rotation profile is displayed by the red dashed curve, while the final profile is shown by the continuous black curve. The thick, blue dashed curve shows a Keplerian angular velocity. The arrow denotes the coordinate radius that contains ~50% of the rest mass of the HMNS (see Figs. 2 and 3). The inset displays the angular velocity in the inner layers of the HMNS.

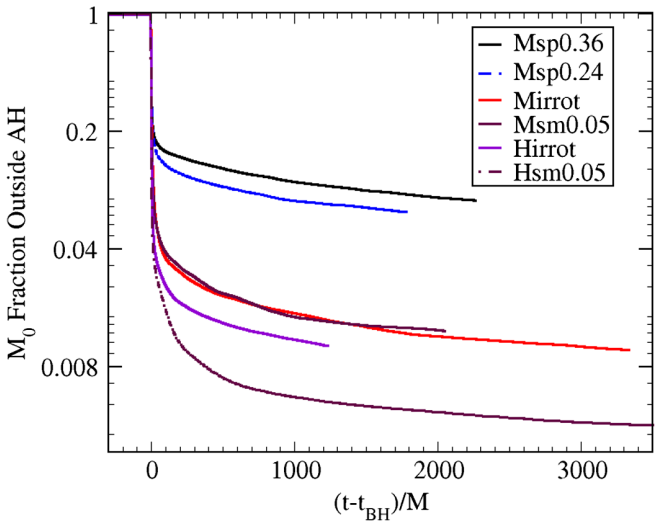

FIG. 6. Rest-mass fraction outside the BH apparent horizon versus time for all cases listed in Table III. The coordinate time has been shifted to the BH formation time $t_{\rm BH}$.

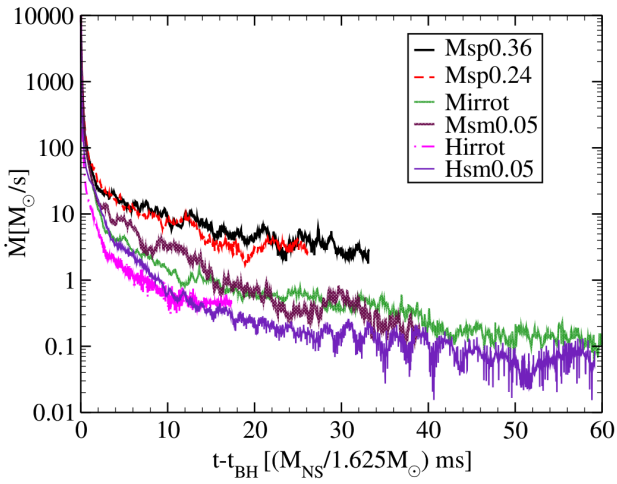

FIG. 7. Rest-mass accretion rate for all cases listed in Table III computed via Eq. (A11) in [88]. The coordinate time has been shifted to the BH formation time $t_{\rm BH}$.

HMNS exceeds the maximum allowed for a uniformly rotating cold star by ∼33%, it can survive only as long as differential rotation in the bulk of the star is maintained.

Nonaxisymmetric matter distributions in the HMNS induce the emission of quasiperiodic GWs and loss of angular momentum (the left panel of Fig. 4). Dissipation of angular momentum due to gravitational radiation is more efficient in cases Hsm0.05 and Hirrot (those with less centrifugal support) than in cases Hsp0.24 or Hsp0.36. In the first two cases we find that $\gtrsim$17% of the total angular momentum is radiated away, while in the two aligned cases it is $\lesssim$13.5% (see Table III). The top panel of Fig. 5 shows the averaged angular velocity profile of the HMNS in cases Hsm0.05 and Hsp0.36 (our extreme cases, see Table I) at different times and within time intervals of length $\Delta t = \pm P_c$ about t, where P_c is its period at birth [see Eq. (2)]. In case Hsm0.05 (similar behavior is observed in case Hirrot), angular momentum is transported from the inner layers of the HMNS to the outer regions (see top right panel in Fig. 5) triggered by torques arising from the nonaxisymmetric structure in the newborn HMNS [99]. We observe that by $t - t_{\rm mer} \simeq 920M \sim 13.5(M_{\rm NS}/1.625\ M_\odot)$ ms the HMNS remnant collapses to a BH (see the bottom right panel in Fig. 2) with a mass of $\sim 2.85(M_{\rm NS}/1.625\ M_\odot)\ M_\odot$ and spin $a/M_{\rm BH} \sim 0.76$ surrounded by a tiny accretion disk (see Fig. 6). By $t - t_{\rm BH} \sim 900M \sim 13(M_{\rm NS}/1.625\ M_\odot)$ ms the accretion rate $\dot{M}$ begins to settle into a quasistationary state and slowly decays thereafter (see Fig. 7). At $t - t_{\rm BH} \sim 1200M \sim 18(M_{\rm NS}/1.625\ M_\odot)$ ms the accretion rate is $\dot{M} \sim 0.4\ M_\odot/s$, and the rest mass of the disk is $0.02\ M_\odot(M_{\rm NS}/1.625\ M_\odot)$. We estimate then that the disk will be accreted in $\tau_{\rm disk} \sim M_{\rm disk}/\dot{M} \sim 41$ ms (see Table III for case Hirrot).

In contrast, in case Hsp0.36 (similar behavior is observed in case Hsp0.24), the high-angular-momentum matter in the bulk of the star rapidly drives the HMNS to a quasiaxisymmetric configuration, reducing the torques that induce angular momentum transport and GW radiation. The top left panel in Fig. 5 shows that after the merger, there are no significant changes in the angular velocity. The newborn HMNS then quickly settles into a quasistationary configuration and remains in quasiequilibrium until the termination of our simulations (see the top right panel in Fig. 2). However, by $t - t_{\rm mer} \approx 3800M \sim 56(M_{\rm NS}/1.625\ M_\odot)$ ms we observe that the minimum value of the lapse slowly begins to decrease. Therefore, the HMNS remnant may be gradually evolving to the point of onset of collapse to a BH.

In most cases, therefore, angular momentum redistributions by nonaxisymmetric torques and gravitational radiation loss are inefficient mechanisms to trigger the collapse of the HMNS remnant. As we will discuss in Sec. III B, other mechanisms, such as magnetic braking and turbulent magnetic viscosity, may be needed to damp the differential rotation in the HMNS and thereby trigger the collapse to a BH [63].

B. Magnetized binaries

As the magnetic-to-gas-pressure ratio in the NS interior is initially small ($\beta^{-1} \sim 10^{-3}$; see Sec. II A), the inspiral dynamics of the magnetized cases proceed basically unperturbed by the magnetic field, though we observe that all the magnetized binaries merge slightly earlier [$\lesssim 200M \sim 3(M_{\rm NS}/1.6\ M_\odot)$ ms] than the corresponding unmagnetized cases (see the right panel of Fig. 4). The stars then simply advect the frozen-in magnetic field lines during the inspiral (see the second row of Fig. 3), and there is no significant changes in the magnetic energy $\mathcal{M}$. Once the NSs make contact, the magnetic energy is steeply enhanced. By $t - t_{\rm mer} \sim 150M \approx 2.2(M_{\rm NS}/1.6\ M_\odot)$ ms

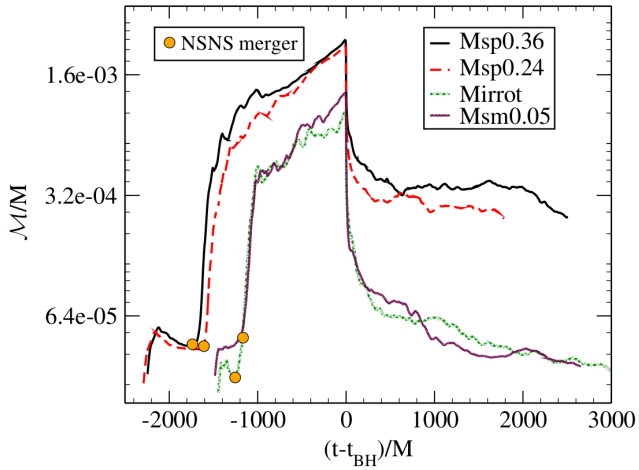

FIG. 8. Total magnetic energy $\mathcal{M}$ normalized by the ADM mass $M = 5.36 \times 10^{54}(M_{NS}/1.625\ M_\odot)$ erg versus time for cases listed in Table III. Dots indicate the NSNS merger time t_{mer}. The coordinate time has been shifted to the BH formation time t_{BH}.

(the time at which the two dense cores merge) the initial magnetic energy already has been amplified by a factor of ∼15 in the two aligned cases, and by a factor of ∼10 in the Msm0.05 and the Mirrot cases (see Fig. 8). Similar behavior was reported in high resolution simulations where it was found that the KH instability, developed during the NSs contact and persisting until the HMNS settles, boost the strength of the magnetic field along with magnetic winding and the MRI [37,82].

Following the merger, high angular momentum matter originating in the outer layers of the newborn HMNS begins to settle in a disk around a central core. As it is shown in the third row of Fig. 3, the mass and size of the disk depend strongly on the initial spin of the NSs. Simultaneously, the inner layers of the star drag the poloidal magnetic field lines into a toroidal configuration (magnetic winding). As the strength of the toroidal magnetic field component is amplified, magnetic stresses increase until they are large enough to redistribute angular momentum and damp the differential rotation [63,100,104]. The winding timescale can be estimated as [see Eq. (2) in [63]]

$$\tau_{\rm wind} \sim \frac{R}{v_A} \sim 10\ {\rm ms}\left(\frac{|B|}{10^{15}\ {\rm G}}\right)^{-1}\left(\frac{R}{10^{6}\ {\rm cm}}\right)\left(\frac{\rho}{10^{14}\ {\rm g/cm^3}}\right)^{1/2}, \quad (3)$$

where R is the characteristic radius of the HMNS and $v_A = |B|/\sqrt{4\pi\rho}$ the Alfvén speed, with $|B|$ the strength of the magnetic field and ρ the characteristic density of the star.

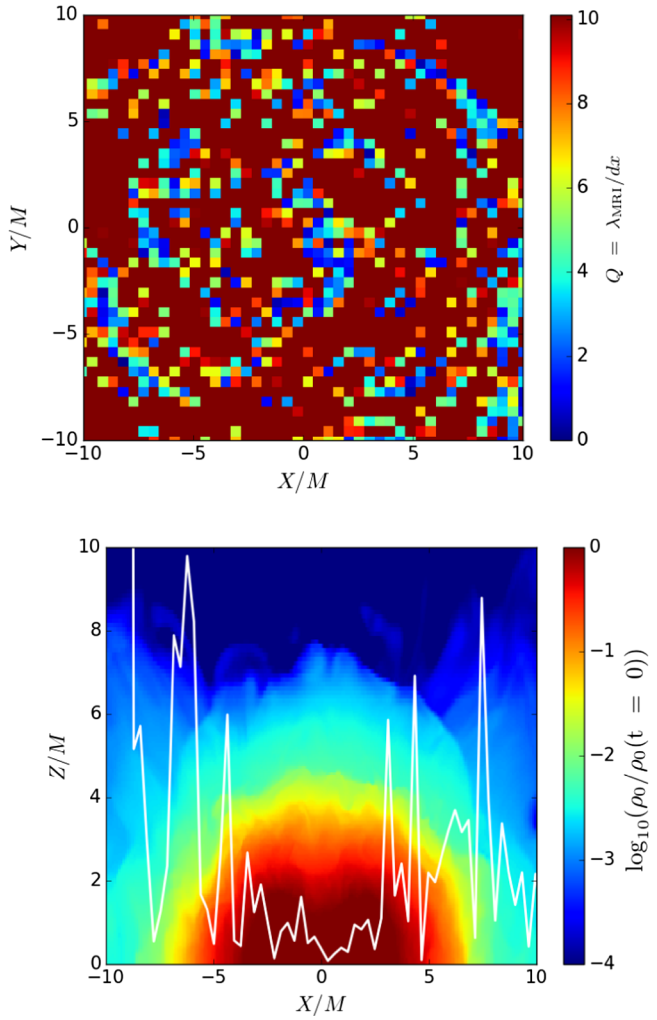

FIG. 9. Contours of the quality factor $Q = \lambda_{\rm MRI}/dx$ on the equatorial plane (top panel), and rest-mass density, normalized to the initial maximum value $\rho_{0,\rm max} \simeq 10^{14.4}(1.625\ M_\odot/M_{NS})^2$ g/cm^3, and $\lambda_{\rm MRI}$ (white line) on the meridional plane (bottom panel) at $t - t_{mer} \sim 400M \sim 6(M_{NS}/1.625\ M_\odot)$ ms for case Msp0.36. We resolve the fastest growing MRI mode by $\gtrsim$10 grid points over a large part of the HMNS. For the most part $\lambda_{\rm MRI}$ fits within the star. Other cases show similar behavior.

We also note that in the HMNS the wavelength $\lambda_{\rm MRI}$ of the fastest growing MRI is resolved by $\gtrsim$10 grid points, and it fits within it (see Fig. 9). Thus, it is likely that the MRI is operating during the lifetime of the HMNS. We also compute the effective Shakura-Sunyaev α_{SS} parameter at $t - t_{mer} \approx 1000M \sim 14.7(M_{NS}/1.6\ M_\odot)$ ms. We find that in the star, the value of α_{SS} ranges between ∼0.01 and ∼0.09 (see Table III). Similar values were reported in high resolution NSNS mergers in [99]. Therefore, it is expected that magnetic turbulence is operating, and it is sustained during the whole lifetime of the HMNS.

Magnetic turbulence can also redistribute angular momentum and damp the differential rotation in a turbulent viscous timescale of [see Eq. (7) in [63]]

$$\tau_{\rm vis} \sim R^{3/2} M^{-1/2} \alpha_{\rm SS}^{-1} \sim 10\ {\rm ms} \left(\frac{\alpha_{\rm ss}}{10^{-2}}\right)^{-1} \left(\frac{M}{3.2\ M_\odot}\right) \left(\frac{\mathcal{C}}{0.3}\right)^{-3/2}, \quad (4)$$

where M is the characteristic mass of the HMNS and $\mathcal{C} = M/R_{\rm eq}$ its compaction, with $R_{\rm eq}$ the equatorial radius of the star. Notice that we have estimated $\tau_{\rm vis}$ using an averaged value of $\alpha_{\rm SS}$ during the whole evolution. However, this timescale can be "locally" as long (short) as $\tau_{\rm vis} \sim 100$ ms ($\tau_{\rm vis} \sim 1$ ms); see Table III. On the other hand, magnetic turbulence can be suppressed by numerical diffusion [99,105,106], and, therefore, the value of $\alpha_{\rm SS}$ in our simulations may be underestimated. Higher resolutions than used here may be required to properly model magnetic turbulence. Nevertheless, it is expected that in higher resolution studies the timescale $\tau_{\rm vis}$ is shortened (see [99,105,106] for a detailed discussion).

Regardless, the angular momentum of the newborn magnetized HMNS, dissipation of angular momentum by gravitational radiation, along with transport angular momentum due to nonaxisymmetric torques, magnetic winding, and magnetic viscosity due to the MRI, cause the contraction of the inner stellar region and the expansion of the external layers. Eventually, the stellar inner region becomes a nearly uniformly rotating massive core immersed in a Keplerian disk (see the bottom panel in Fig. 5). By $t - t_{\rm mer} \lesssim 1400M \sim 20.5(M_{\rm NS}/1.625\ M_\odot)$ ms after merger the HMNS collapses (see Table III) as first demonstrated in [107]. We find that the larger the spin the smaller the mass of the remnant BH and, therefore, the heavier the disk (see Fig. 6). However, in all cases the BH dimensionless spin is $a/M_{\rm BH} \simeq 0.78$ (see Table III). The independence of the nascent BH spin on the initial NS spin may be an EOS-independent outcome. We plan to investigate this further in future work. Magnetic winding and MRI will transport angular momentum as long as the matter is differentially rotating. So, the HMNS will be driven into a massive central core + disk configuration in a timescale that depends only on how much angular momentum needs to be extracted from the inner stellar region and deposited in the outermost layers [see Eqs. (3) and (4)]. Note that in the high resolution case reported in [10] the remnant BH has a spin $a/M_{\rm BH} \simeq 0.74$, though that case corresponds to the irrotational case in Table I with a poloidal magnetic field confined to the NS interior. High resolutions are therefore required to accurately determine the final spin of the BH remnant. Notice that in cases Msm0.05 and Mirrot, the HMNS collapses to a BH later than its hydrodynamic counterpart (see Table III): due to magnetic turbulence, kinetic energy is dissipated through small scale shocks which heat up the star, thus increasing the thermal pressure support compared to the scenario without magnetic fields.

During HMNS collapse, the inner layers of the star, which contain most of the magnetic energy, are promptly accreted into the BH. The magnetic energy $\mathcal{M}$ then plummets in only $t - t_{\rm BH} \sim 50{\rm M} \sim 0.7(M_{\rm NS}/1.625\ M_\odot)$ ms following collapse, and then slightly decreases thereafter as the accretion proceeds (see Fig. 8). As magnetic winding during the lifetime of the HMNS allows the magnetic energy to reach equipartition levels [82], the magnetic field does not grow in the disk following BH formation [10]. After HMNS collapse, we find that the rms value of the magnetic field in the disk is $\lesssim 10^{16}(1.625\ M_\odot/M_{\rm NS})$ G (see Table III).

Although immediately after BH formation the atmosphere is a very gas-loaded environment [108], the winding of the magnetic field above the BH poles has been well underway even before collapse (see the fourth row in Fig. 3). By $t - t_{\rm BH} \sim 2000M \sim 30(M_{\rm NS}/1.625\ M_\odot)$ ms in cases Msm0.05 and Mirrot, and $t - t_{\rm BH} \sim 1000M \sim 15(M_{\rm NS}/1.625\ M_\odot)$ ms in the aligned cases, the magnetic pressure above the BH poles balances the ram pressure of the fallback debris and the inflow stops. Fluid velocities then start to turn around and point outward. Simultaneously, the magnetic field is tightly wound into a helical funnel (see the bottom panels in Fig. 3). As the regions above the BH poles are cleaned out, magnetically dominated regions $[b^2/(2\rho_0) \gtrsim 1]$ in the funnel gradually start to expand. Once $b^2/(2\rho_0) \gtrsim 10$, the magnetic pressure above the BH poles is high enough to overcome the ram pressure, and a magnetically sustained outflow emerges. In all cases, we observe that at about $t \sim 850M - 900M \sim 12.513(M_{\rm NS}/1.625\ M_\odot)$ ms $- 13(M_{\rm NS}/1.625\ M_\odot)$ ms after the fluid velocities change direction for the first time, the outflow reaches heights $\geq 100M \sim 430(M_{\rm NS}/1.625\ M_\odot)$ km, and the Lorentz factor inside the funnel is $\Gamma_L \sim 1.1$–1.3. Thus, at $\sim 3000M - 4000M \sim 45(M_{\rm NS}/1.625\ M_\odot)$ ms $- 60({\rm M_{NS}}/1.625\ {\rm M_\odot})$ ms following the NSNS merger a magnetically driven and mildly relativistic outflow—*an incipient jet*—has been launched (see Table III). Note that the jet near the poles is only mildly relativistic. However, as it is shown in Fig. 10 the ratio $b^2/(2\rho_0)$ above the BH poles is $\gtrsim 100$. The maximum feasible Lorentz factor Γ_L for Poynting-dominated jets equals $b^2/(2\rho_0)$ [109]. So, matter in the funnel of the incipient jet can be accelerated to $\Gamma_L \gtrsim 100$, as required by sGRB models.

To determine the collimation of the jet, we estimate the funnel opening angle $\theta_{\rm jet}$ using the $b^2/(2\rho_0) \sim 10^{-2}$ contour as the boundary of the funnel [10]. In all cases, we find that the funnel opening angle is $\sim 25°$–$30°$ (see Fig. 10). Figure 7 shows the accretion disk history for all cases. In the aligned cases, the accretion reaches a quasistationary state at about $t - t_{\rm BH} \sim 1000M \sim 15(M_{\rm NS}/1.625\ M_\odot)$ ms, while in the other two cases the quasistationary state is reached at roughly $t - t_{\rm BH} \sim 1350M \sim 20(M_{\rm NS}/1.625\ M_\odot)$ ms. Based on the accretion rate at $t - t_{\rm BH} \sim 2000M \sim 30(M_{\rm NS}/1.625\ M_\odot)$ ms and the mass of the accretion disk (see Fig. 7), we estimate that the disk will be accreted in $\Delta t \sim M_{\rm disk}/\dot{M} \gtrsim 98$ ms (see Table III),

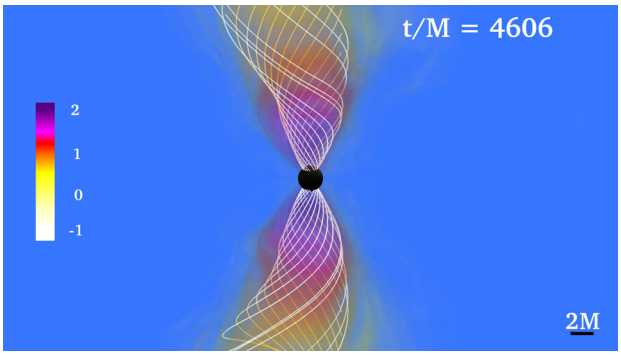

FIG. 10. Volume rendering of the ratio $b^2/2\rho_0$ (log scale) at $t - t_{\rm BH} \approx 3400M \sim 50(M_{\rm NS}/1.625\ M_\odot)$ ms for the Mirrot case, though similar behavior is observed in all magnetized cases. Magnetic field lines (white lines) are plotted inside regions where $b^2/2\rho_0 \gtrsim 10^{-2}$ (funnel boundary). Magnetically dominated regions ($b^2/2\rho_0 \gtrsim 1$) extend to heights $\gtrsim 20M \sim 20 r_{\rm BH}$ above the BH (black sphere). Here $r_{\rm BH} = 2.2(M_{\rm NS}/1.625\ M_\odot)$ km.

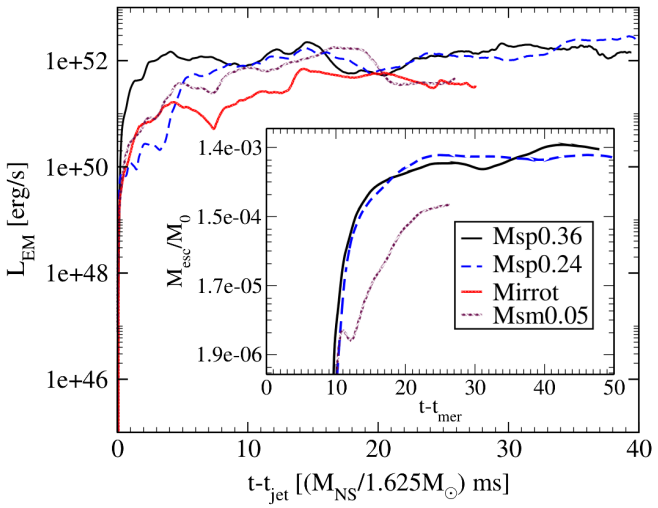

FIG. 11. Outgoing EM (Poynting) luminosity for $t \geq t_{\rm jet}$ computed at a coordinate sphere of radius $r = 120M \sim 530(M_{\rm NS}/1.625\ M_\odot)$ km for the magnetized cases listed in Table III. The inset shows the rest-mass fraction of escaping matter during the last $\sim 2700M \sim 40(M_{\rm NS}/1.625\ M_\odot)$ ms before the termination of our simulations.

the timescale consistent with those of typical short-duration sGRBs (see e.g., [110]).

To verify if the BZ mechanism is operating in our simulations, we compare the outgoing Poynting luminosity $L_{\rm EM}$ computed across a spherical surface of coordinate radius of $r_{\rm ext} \approx 120M \sim 530(M_{\rm NS}/1.625\ M_\odot)$ km (see Sec. II C) to the expected EM power generated by the BZ mechanism given by [111]

$$L_{\rm BZ} \sim 10^{52} \left(\frac{a/M_{\rm BH}}{0.75}\right)^2 \left(\frac{M_{\rm BH}}{2.8\ M_\odot}\right)^2 \left(\frac{|B|}{10^{16}\ {\rm G}}\right)^2 {\rm erg/s}. \quad (5)$$

As it is shown in Fig. 11, the Poynting luminosity is $L_{\rm EM} \sim 10^{51\pm1}$ erg/s (see Table III for a time-averaged value over the last $500M \sim 7.4(M_{\rm NS}/1.625\ M_\odot)$ ms before the termination of our simulations when the jet is well developed), roughly consistent with the expected $L_{\rm BZ}$ value in Eq. (5). In addition, we also compute the ratio of the angular velocity of the magnetic field to the angular velocity of the BH, Ω_F/Ω_H, on a meridional plane passing through the apparent horizon centroid (see e.g., [112]). We find that inside the funnel Ω_F/Ω_H ranges from ~0.3 to 0.6. As it has been pointed out in [8,113], deviations from the expected value $\Omega_F/\Omega_H = 0.5$ for an idealized monopole field [114] may be due to numerical artifacts or deviations from strict force-free behavior. The above values along with the tightly wound helical magnetic field above the BH poles suggest that the BZ mechanism is likely operating in the BH + disk remnants. We also compute the BZ power efficiency $\eta_{\rm eff} = L_{\rm EM}/\dot{M}$, time averaged over the last $t \sim 500M \sim 7.4(M_{\rm NS}/1.625\ M_\odot)$ ms before the termination of our simulations. In all our models, we find that $\eta_{\rm eff} \sim 0.3\%$ (see Table III) are consistent with BH + disk GRMHD simulations for BHs with similar spins [see Eq. (3) in [115]]. Note that the resulting luminosities and accretion rates are also consistent with the "universal model" common to all BH + disk systems formed following magnetized BHNS and NSNS mergers and magnetorotational stellar collapse [116].

As it has been pointed out in [87], matter ejection in NSNS mergers $\gtrsim 10^{-3}\ M_\odot$ are required for detectable kilonovae. The inset of Fig. 11 shows the rest-mass fraction of escaping matter during the last $\sim 2700M \sim 40(M_{\rm NS}/1.625\ M_\odot)$ ms out to our outer boundaries [$\sim 1100(M_{\rm NS}/1.625\ M_\odot)$ km] before the termination of our simulations. Our calculation does not account for the ejected material that has left the numerical domain by that time. Hence, our reported values indicate a *lower limit* on the ejected material. In our two aligned cases we find that the rest-mass fraction $M_{\rm esc}$ of the escaping mass is $\gtrsim 10^{-2.3}(M_{\rm NS}/1.625\ M_\odot)\ M_\odot$ (see inset of Fig. 11). So, in principle, the radioactive decay of the above ejecta will power a light curve with a luminosity of $\sim 10^{42}$ erg/s and, therefore, could be detected by current telescopes, as well as the LSST [47,64].

IV. CONCLUSIONS

The likely assumption that the progenitor of GW170817 was a merging NSNS system, along with the multiple counterpart radiation observations across the EM spectrum, allows us to impose constraints on the maximum mass of a nonrotating star [43,44,47,48], on the radius of the NS [1,117–121], and the EOS (see e.g., [120,122–124] and references therein). However, an open question for GW170817 remains the impact of the initial NS spins on the outcome of the merger. These could have a strong

impact on the remnant disk, the final BH spin, the lifetime of the transient HMNS, the amount of ejected neutron rich matter that can power kilonovae and synthesize heavy elements, and the formation and lifetime of a magnetically driven jet and the associated outgoing EM Poynting luminosity. To address these issues, here we initiate GRMHD simulations of different NSNS configurations undergoing merger and delayed collapse to a BH while accounting for the initial NS spin. The binaries consist of two identical stars, in quasicircular orbit, each with spins $\chi_{\rm NS} = -0.053$, 0, 0.24, or 0.36. In this first exploratory work we model the initial stars with a $\Gamma = 2$ polytropic EOS. To determine the impact of the magnetically driven effects on the fate of a spinning NSNS remnant, we have also considered unmagnetized evolution of the above NSNS configurations.

We found that following the NSNS merger, the redistribution of angular momentum due mainly to magnetic braking by winding and magnetic turbulence driven by the MRI in the bulk of the transient HMNS remnant, along with the angular momentum dissipation due to gravitational radiation, induces the formation of a massive, nearly uniformly rotating inner core immersed in a Keplerian disklike envelope. Eventually the HMNS collapses to a BH with a final spin $a/M_{\rm BH} \simeq 0.78$ almost independent of the initial NS spin. In our unmagnetized cases with high aligned spins the merger product is a long-lived HMNS (in contrast to the aligned spin magnetized models) while the irrotational and antialigned spinning ones collapse to a BH in agreement with the pure hydrodynamic simulations of [55,56] which used constraint violating spinning initial conditions. Regarding the unmagnetized binaries, because of our relative low-mass priors we could not verify the argument made by [55,56] about the increase of the BH spin *vis-à-vis* the initial spin of the NSs, and further work is needed toward that direction. On the other hand, the existence of a magnetic field triggers delayed collapse [within $15(M_{\rm NS}/1.625\ M_\odot)$ ms] in the case of sufficiently low-mass remnants. The final BH in our simulations is surrounded by a magnetized accretion disk whose rest mass depends strongly on the initial spin of the NSs. Our numerical results indicate that the excess of angular momentum is deposited in the exterior layers to form the accretion disk. Thus, the larger the initial spin of NSs the heavier the disk. We anticipate that the above behavior will remain substantially unchanged when alternative EOSs are used to model the NSs. Magnetic winding and MRI will transport angular momentum as long as the matter is differentially rotating. The HMNS will then be driven into a massive central core + disk configuration in a timescale that depends only on how much angular momentum needs to be extracted from the inner stellar region and deposited in the outermost layers before centrifugal support is no longer adequate to support the star against collapse [see Eqs. (3) and (4)].

After $\Delta t \sim 3000M - 4000M \sim 45(M_{\rm NS}/1.625\,M_\odot)$ ms – $60(\mathrm{M_{NS}}/1.625\,\mathrm{M_\odot})$ ms following the merger, a magnetically driven and sustained incipient jet is launched. The lifetime of the jets [$\Delta t \sim 100(M_{\rm NS}/1.625\ M_\odot)$ ms – $140(M_{\rm NS}/1.625\ M_\odot)$ ms] and their outgoing Poynting luminosities [$L_{\rm EM} \sim 10^{51.5\pm1}$ erg/s] are consistent with short-duration sGRBs [32–34], as well as with the BZ process for launching jets and their associated Poynting luminosities. The low luminosity of GW170817 [$L \sim 10^{47}$ erg/s] is best understood by recent calculations showing that the jet is misaligned with our line of sight by 20°–30° [125].

In the unmagnetized cases, we found that, by contrast with the HMNS in the antialigned and irrotational configurations that undergo delayed collapse to a BH after about $\sim 13(M_{\rm NS}/1.625\ M_\odot)$ ms following merger, the HMNS in the aligned cases is driven to a quasiaxisymmetric configuration on a dynamical timescale, and it remains in quasistationary equilibrium until the termination of our simulations [$t - t_{\rm mer} \gtrsim 50(M_{\rm NS}/1.625\ M_\odot)$ ms]. Angular momentum redistribution by internal torques and dissipation due to gravitational radiation alone are, therefore, inefficient mechanisms to trigger the collapse of a highly spinning HMNS.

ACKNOWLEDGMENTS

We thank the Illinois Relativity REU team (G. Liu, K. Nelli, and M. Nguyen) for assistance with some of the visualizations. This work has been supported in part by National Science Foundation (NSF) Grant No. PHY-1662211 and NASA Grant No. 80NSSC17K0070 at the University of Illinois at Urbana-Champaign. This work made use of the Extreme Science and Engineering Discovery Environment (XSEDE), which is supported by National Science Foundation Grant No. TG-MCA99S008. This research is part of the Blue Waters sustained-petascale computing project, which is supported by the National Science Foundation (Grants No. OCI-0725070 and No. ACI-1238993) and the State of Illinois. Blue Waters is a joint effort of the University of Illinois at Urbana-Champaign and its National Center for Supercomputing Applications.

[1] B. P. Abbott *et al.* (Virgo and LIGO Scientific Collaboration), Phys. Rev. Lett. **119**, 161101 (2017).
[2] A. von Kienlin, C. Meegan, and A. Goldstein, GRB coordinates network, circular service, no. 21520, #1 1520 (2017).
[3] V. Savchenko *et al.*, Astrophys. J. **848**, L15 (2017).
[4] V. Savchenko *et al.*, LIGO/Virgo G298048: INTEGRAL detection of a prompt gamma-ray counterpart, no. 21507, #1 (2017).
[5] B. Paczynski, Astrophys. J. **308**, L43 (1986).
[6] D. Eichler, M. Livio, T. Piran, and D. N. Schramm, Nature (London) **340**, 126 (1989).
[7] R. Narayan, B. Paczynski, and T. Piran, Astrophys. J. Lett. **395**, L83 (1992).
[8] V. Paschalidis, M. Ruiz, and S. L. Shapiro, Astrophys. J. **806**, L14 (2015).
[9] M. Ruiz, S. L. Shapiro, and A. Tsokaros, Phys. Rev. D **98**, 123017 (2018).
[10] M. Ruiz, R. N. Lang, V. Paschalidis, and S. L. Shapiro, Astrophys. J. **824**, L6 (2016).
[11] M. Ruiz and S. L. Shapiro, Phys. Rev. D **96**, 084063 (2017).
[12] F. Özel and P. Freire, Annu. Rev. Astron. Astrophys. **54**, 401 (2016).
[13] J. M. Lattimer and M. Prakash, Phys. Rep. **621**, 127 (2016).
[14] B. P. Abbott *et al.*, Astrophys. J. **848**, L12 (2017).
[15] H. Yang, W. E. East, and L. Lehner, Astrophys. J. **856**, 110 (2018).
[16] T. Hinderer *et al.*, arXiv:1808.03836.
[17] F. Foucart, T. Hinderer, and S. Nissanke, Phys. Rev. D **98**, 081501 (2018).
[18] M. W. Coughlin and T. Dietrich, arXiv:1901.06052.
[19] R. Popham, S. E. Woosley, and C. Fryer, Astrophys. J. **518**, 356 (1999).
[20] T. Di Matteo, R. Perna, and R. Narayan, Astrophys. J. **579**, 706 (2002).
[21] W.-X. Chen and A. M. Beloborodov, Astrophys. J. **657**, 383 (2007).
[22] W.-H. Lei, B. Zhang, and E.-W. Liang, Astrophys. J. **765**, 125 (2013).
[23] O. Just, M. Obergaulinger, H. T. Janka, A. Bauswein, and N. Schwarz, Astrophys. J. **816**, L30 (2016).
[24] W.-H. Lei, B. Zhang, X.-F. Wu, and E.-W. Liang, Astrophys. J. **849**, 47 (2017).
[25] R. D. Blandford and R. L. Znajek, Mon. Not. R. Astron. Soc. **179**, 433 (1977).
[26] F. F. Dirirsa (Fermi-LAT Collaboration), Proc. Sci., HEASA2016 (**2017**) 004.
[27] Note that it has been suggested [28,29] that NSNS undergoing prompt collapse to a BH may be the progenitors of fast radio bursts, a new class of radio transients lasting between a few to a couple of tens of milliseconds [30,31].
[28] T. Totani, Publ. Astron. Soc. Jpn. **65**, L12 (2013).
[29] V. Paschalidis and M. Ruiz, arXiv:1808.04822.
[30] D. R. Lorimer, M. Bailes, M. A. McLaughlin, D. J. Narkevic, and F. Crawford, Science **318**, 777 (2007).
[31] D. Thornton *et al.*, Science **341**, 53 (2013).
[32] P. N. Bhat *et al.*, Astrophys. J. Suppl. Ser. **223**, 28 (2016).
[33] A. Lien *et al.*, Astrophys. J. **829**, 7 (2016).
[34] D. S. Svinkin, D. D. Frederiks, R. L. Aptekar, S. V. Golenetskii, V. D. Pal'shin, P. P. Oleynik, A. E. Tsvetkova, M. V. Ulanov, T. L. Cline, and K. Hurley, Astrophys. J. Suppl. Ser. **224**, 10 (2016).
[35] T. Kawamura, B. Giacomazzo, W. Kastaun, R. Ciolfi, A. Endrizzi, L. Baiotti, and R. Perna, Phys. Rev. D **94**, 064012 (2016).
[36] R. Ciolfi, W. Kastaun, B. Giacomazzo, A. Endrizzi, D. M. Siegel, and R. Perna, Phys. Rev. D **95**, 063016 (2017).
[37] K. Kiuchi, K. Kyutoku, Y. Sekiguchi, M. Shibata, and T. Wada, Phys. Rev. D **90**, 041502 (2014).
[38] V. Paschalidis, Classical Quantum Gravity **34**, 084002 (2017).
[39] A. Perego, H. Yasin, and A. Arcones, J. Phys. G **44**, 084007 (2017).
[40] M. Shibata and K. Uryu, Prog. Theor. Phys. **107**, 265 (2002).
[41] M. Shibata, K. Taniguchi, and K. Uryu, Phys. Rev. D **68**, 084020 (2003).
[42] M. Shibata and K. Taniguchi, Phys. Rev. D **73**, 064027 (2006).
[43] B. Margalit and B. D. Metzger, Astrophys. J. **850**, L19 (2017).
[44] M. Ruiz, S. L. Shapiro, and A. Tsokaros, Phys. Rev. D **97**, 021501 (2018).
[45] J. L. Friedman and J. R. Ipser, Astrophys. J. **314**, 594 (1987).
[46] S. Koranda, N. Stergioulas, and J. L. Friedman, Astrophys. J. **488**, 799 (1997).
[47] M. Shibata, S. Fujibayashi, K. Hotokezaka, K. Kiuchi, K. Kyutoku, Y. Sekiguchi, and M. Tanaka, Phys. Rev. D **96**, 123012 (2017).
[48] L. Rezzolla, E. R. Most, and L. R. Weih, Astrophys. J. **852**, L25 (2018).
[49] L. Piro *et al.*, Mon. Not. R. Astron. Soc. **483**, 1912 (2019).
[50] S. Bernuzzi, T. Dietrich, W. Tichy, and B. Bruegmann, Phys. Rev. D **89**, 104021 (2014).
[51] N. Tacik *et al.*, Phys. Rev. D **92**, 124012 (2015); **94**, 049903(E) (2016).
[52] T. Dietrich, S. Bernuzzi, M. Ujevic, and W. Tichy, Phys. Rev. D **95**, 044045 (2017).
[53] T. Dietrich, N. Moldenhauer, N. K. Johnson-McDaniel, S. Bernuzzi, C. M. Markakis, B. Brgmann, and W. Tichy, Phys. Rev. D **92**, 124007 (2015).
[54] T. Dietrich, S. Bernuzzi, B. Brgmann, M. Ujevic, and W. Tichy, Phys. Rev. D **97**, 064002 (2018).
[55] W. Kastaun, F. Galeazzi, D. Alic, L. Rezzolla, and J. A. Font, Phys. Rev. D **88**, 021501 (2013).
[56] W. Kastaun and F. Galeazzi, Phys. Rev. D **91**, 064027 (2015).
[57] A. Bauswein, N. Stergioulas, and H.-T. Janka, Eur. Phys. J. **A52**, 56 (2016).
[58] W. E. East, V. Paschalidis, and F. Pretorius, Astrophys. J. **807**, L3 (2015).
[59] V. Paschalidis, W. E. East, F. Pretorius, and S. L. Shapiro, Phys. Rev. D **92**, 121502 (2015).
[60] W. E. East, V. Paschalidis, F. Pretorius, and S. L. Shapiro, Phys. Rev. D **93**, 024011 (2016).

[61] W. E. East, V. Paschalidis, and F. Pretorius, Classical Quantum Gravity **33**, 244004 (2016).
[62] A. Tsokaros, K. Uryu, M. Ruiz, and S. L. Shapiro, Phys. Rev. D **98**, 124019 (2018).
[63] L. Sun, M. Ruiz, and S. L. Shapiro, Phys. Rev. D **99**, 064057 (2019).
[64] S. Rosswog, Astrophys. J. **634**, 1202 (2005).
[65] G. Allen, D. Angulo, I. Foster, G. Lanfermann, C. Liu, T. Radke, E. Seidel, and J. Shalf, Int. J. High Perform. Comput. Appl. **15**, 345 (2001).
[66] Cactus, Cactuscode, http://cactuscode.org/.
[67] M. Shibata and T. Nakamura, Phys. Rev. D **52**, 5428 (1995).
[68] T. W. Baumgarte and S. L. Shapiro, Phys. Rev. D **59**, 024007 (1998).
[69] T. W. Baumgarte and S. L. Shapiro, *Numerical Relativity: Solving Einstein's Equations on the Computer* (Cambridge University Press, Cambridge, England, 2010).
[70] Z. B. Etienne, J. A. Faber, Y. T. Liu, S. L. Shapiro, K. Taniguchi, and T. W. Baumgarte, Phys. Rev. D **77**, 084002 (2008).
[71] M. D. Duez, P. Marronetti, S. L. Shapiro, and T. W. Baumgarte, Phys. Rev. D **67**, 024004 (2003).
[72] E. Schnetter, S. H. Hawley, and I. Hawke, Classical Quantum Gravity **21**, 1465 (2004).
[73] Carpet, http://www.carpetcode.org/, Carpet Code Homepage.
[74] J. G. Baker, J. Centrella, D.-I. Choi, M. Koppitz, and J. van Meter, Phys. Rev. D **73**, 104002 (2006).
[75] Z. B. Etienne, Y. T. Liu, and S. L. Shapiro, Phys. Rev. D **82**, 084031 (2010).
[76] B. D. Farris, R. Gold, V. Paschalidis, Z. B. Etienne, and S. L. Shapiro, Phys. Rev. Lett. **109**, 221102 (2012).
[77] Z. B. Etienne, V. Paschalidis, Y. T. Liu, and S. L. Shapiro, Phys. Rev. D **85**, 024013 (2012).
[78] A. Tsokaros, K. Ury, and L. Rezzolla, Phys. Rev. D **91**, 104030 (2015).
[79] T. Hinderer, Astrophys. J. **677**, 1216 (2008).
[80] T. Hinderer, B. D. Lackey, R. N. Lang, and J. S. Read, Phys. Rev. D **81**, 123016 (2010).
[81] V. Paschalidis, Z. B. Etienne, and S. L. Shapiro, Phys. Rev. D **88**, 021504 (2013).
[82] K. Kiuchi, P. Cerd-Durn, K. Kyutoku, Y. Sekiguchi, and M. Shibata, Phys. Rev. D **92**, 124034 (2015).
[83] J. A. Font, Living Rev. Relativity **11**, 7 (2008).
[84] J. Thornburg, Classical Quantum Gravity **21**, 743 (2004).
[85] O. Dreyer, B. Krishnan, D. Shoemaker, and E. Schnetter, Phys. Rev. D **67**, 024018 (2003).
[86] M. Ruiz, R. Takahashi, M. Alcubierre, and D. Nunez, Gen. Relativ. Gravit. **40**, 2467 (2008).
[87] B. D. Metzger and E. Berger, Astrophys. J. **746**, 48 (2012).
[88] B. D. Farris, Y. T. Liu, and S. L. Shapiro, Phys. Rev. D **81**, 084008 (2010).
[89] Z. B. Etienne, Y. T. Liu, V. Paschalidis, and S. L. Shapiro, Phys. Rev. D **85**, 064029 (2012).
[90] N. I. Shakura and R. A. Sunyaev, Astron. Astrophys. **24**, 337 (1973).
[91] R. F. Penna, J. C. McKinney, R. Narayan, A. Tchekhovskoy, R. Shafee, and J. E. McClintock, Mon. Not. R. Astron. Soc. **408**, 752 (2010).
[92] Z. B. Etienne, V. Paschalidis, and S. L. Shapiro, Phys. Rev. D **86**, 084026 (2012).
[93] T. Sano, S.-i. Inutsuka, N. J. Turner, and J. M. Stone, Astrophys. J. **605**, 321 (2004).
[94] H. Shiokawa, J. C. Dolence, C. F. Gammie, and S. C. Noble, Astrophys. J. **744**, 187 (2012).
[95] M. Hanauske, K. Takami, L. Bovard, L. Rezzolla, J. A. Font, F. Galeazzi, and H. Stcker, Phys. Rev. D **96**, 043004 (2017).
[96] W. Kastaun and F. Galeazzi, Phys. Rev. D **91**, 064027 (2015).
[97] G. B. Cook, S. L. Shapiro, and S. A. Teukolsky, Astrophys. J. **422**, 227 (1994).
[98] N. D. Lyford, T. W. Baumgarte, and S. L. Shapiro, Astrophys. J. **583**, 410 (2003).
[99] K. Kiuchi, K. Kyutoku, Y. Sekiguchi, and M. Shibata, Phys. Rev. D **97**, 124039 (2018).
[100] S. L. Shapiro, Astrophys. J. **544**, 397 (2000).
[101] K. Kiuchi, Y. Sekiguchi, K. Kyutoku, M. Shibata, K. Taniguchi, and T. Wada, Phys. Rev. D **92**, 064034 (2015).
[102] M. Campanelli, C. O. Lousto, and Y. Zlochower, Phys. Rev. D **74**, 041501 (2006).
[103] M. Shibata and K. Uryū, Phys. Rev. D **61**, 064001 (2000).
[104] M. D. Duez, Y. T. Liu, S. L. Shapiro, M. Shibata, and B. C. Stephens, Phys. Rev. Lett. **96**, 031101 (2006).
[105] J. F. Hawley, X. Guan, and J. H. Krolik, Astrophys. J. **738**, 84 (2011).
[106] J. F. Hawley, S. A. Richers, X. Guan, and J. H. Krolik, Astrophys. J. **772**, 102 (2013).
[107] M. D. Duez, Y. T. Liu, S. L. Shapiro, and B. C. Stephens, Phys. Rev. D **69**, 104030 (2004).
[108] O. Just, M. Obergaulinger, H.-T. Janka, A. Bauswein, and N. Schwarz, Astrophys. J. **816**, L30 (2016).
[109] N. Vlahakis and A. Königl, Astrophys. J. **596**, 1080 (2003).
[110] D. A. Kann *et al.*, Astrophys. J. **734**, 96 (2011).
[111] K. S. Thorne, R. H. Price, and D. A. Macdonald, *The Membrane Paradigm* (Yale University Press, New Haven, 1986).
[112] J. C. McKinney and C. F. Gammie, Astrophys. J. **611**, 977 (2004).
[113] J. C. McKinney and C. F. Gammie, Astrophys. J. **611**, 977 (2004).
[114] R. D. Blandford and R. L. Znajek, Mon. Not. R. Astron. Soc. **179**, 433 (1977).
[115] J. C. McKinney, Astrophys. J. **630**, L5 (2005).
[116] S. L. Shapiro, Phys. Rev. D **95**, 101303 (2017).
[117] A. Bauswein, O. Just, H.-T. Janka, and N. Stergioulas, Astrophys. J. **850**, L34 (2017).
[118] D. Radice, A. Perego, F. Zappa, and S. Bernuzzi, Astrophys. J. **852**, L29 (2018).
[119] E. R. Most, L. R. Weih, L. Rezzolla, and J. Schaffner-Bielich, Phys. Rev. Lett. **120**, 261103 (2018).
[120] B. P. Abbott *et al.* (Virgo and LIGO Scientific Collaborations), Phys. Rev. Lett. **121**, 161101 (2018).
[121] C. Raithel, F. zel, and D. Psaltis, Astrophys. J. **857**, L23 (2018).

[122] E. Annala, T. Gorda, A. Kurkela, and A. Vuorinen, Phys. Rev. Lett. **120**, 172703 (2018).
[123] V. Paschalidis, K. Yagi, D. Alvarez-Castillo, D. B. Blaschke, and A. Sedrakian, Phys. Rev. D **97**, 084038 (2018).
[124] S. De, D. Finstad, J. M. Lattimer, D. A. Brown, E. Berger, and C. M. Biwer, Phys. Rev. Lett. **121**, 091102 (2018); **121**, 259902 (2018).
[125] B. P. Abbott *et al.* (Virgo, Fermi-GBM, INTEGRAL, LIGO Scientific Collaborations), Astrophys. J. **848**, L13 (2017).